AGU ADVANCING EARTH AND SPACE SCIENCE

Geophysical Research Letters®

RESEARCH LETTER
10.1029/2022GL101173

InSAR-Derived Horizontal Velocities in a Global Reference Frame

M. Lazecký[1], A. J. Hooper[1], and P. Piromthong[1,2]

[1]COMET, School of Earth and Environment, University of Leeds, Leeds, UK, [2]Survey Engineering, Faculty of Engineering, Chulalongkorn University, Bangkok, Thailand

Key Points:

- We can use Sentinel-1 InSAR to measure along-track velocities over wide areas in a global reference frame
- Horizontal velocity vectors can be estimated, which generally agree with the ITRF2014 plate motion model and global GPS network estimates
- The updated Sentinel-1 precise orbits introduced in mid-2020 improve the model accuracy and induce a single offset

Supporting Information:

Supporting Information may be found in the online version of this article.

Correspondence to:

M. Lazecký,
M.Lazecky@leeds.ac.uk

Citation:

Lazecký, M., Hooper, A. J., & Piromthong, P. (2023). InSAR-derived horizontal velocities in a global reference frame. *Geophysical Research Letters*, *50*, e2022GL101173. https://doi.org/10.1029/2022GL101173

Received 9 SEP 2022
Accepted 18 APR 2023

Author Contributions:

Conceptualization: M. Lazecký, A. J. Hooper
Data curation: M. Lazecký
Formal analysis: A. J. Hooper
Investigation: M. Lazecký, P. Piromthong
Methodology: M. Lazecký, A. J. Hooper
Resources: M. Lazecký
Software: M. Lazecký
Supervision: A. J. Hooper
Validation: M. Lazecký
Visualization: M. Lazecký
Writing – original draft: M. Lazecký
Writing – review & editing: A. J. Hooper

Abstract Interferometric Synthetic Aperture Radar is used to measure deformation rates over continents to constrain tectonic processes. The resulting velocity measurements are only relative, however, due to unknown integer ambiguities introduced during propagation of the signal through the atmosphere. These ambiguities mostly cancel when using spectral diversity to estimate along-track motion, allowing measurements to be made with respect to a global reference frame. Here, we calculate along-track velocities for a partial global data set of Sentinel-1 acquisitions and find good agreement with ITRF2014 plate motion model and measurements from GPS stations. We include corrections for solid-earth tides and gradients of ionospheric total electron content. Combining data from ascending and descending orbits we are able to estimate north and east velocities over 250 × 250 km areas and their accuracy of 4 and 23 mm/year, respectively. These "absolute" measurements can be particularly useful for global velocity and strain rate estimation where GNSS measurements are sparse.

Plain Language Summary It is possible to use repeated radar measurements from satellites to measure movement of the ground toward or away from the satellite very accurately. These measurements do not tell us the absolute movement, however, but rather the difference in movement between any two parts of the ground captured in the same radar image. Using a related technique, we measure horizontal movement of the ground in the flight direction of the satellite, and these are absolute measurements, in a global reference frame. By combining measurements from different flight directions, we can estimate the horizontal movement of the ground in any direction. Our estimates largely match what we expect from plate tectonics and measurements made using GPS instruments. These new measurements can be useful for large-scale mapping of ground movement, which can be used to better understand how the Earth deforms and how earthquake hazard varies across the globe.

1. Introduction

With the launch of the Copernicus Sentinel-1 Synthetic Aperture Radar (SAR) mission, the geoscience community acquired a unique tool for making precise measurements of large-scale surface deformation. The Center for Observation and Modeling of Earthquakes, Volcanoes and Tectonics (COMET) LiCSAR system (Lazecký et al., 2020) routinely generates Sentinel-1 differential interferograms over tectonic and volcanic areas, and carries out interferometric (InSAR) time series analyses to measure surface deformation in the satellite line-of-sight direction. When the satellites are traveling south to north (ascending), the look direction is downwards and slightly north of eastwards, and when moving north to south (descending) it is downwards and slightly north of westwards. The two geometries can therefore be used to accurately constrain the vertical and east-west components of any motion, but the line-of-sight sensitivity is very low for the north-south component, which is typically estimated using available GNSS data (Weiss et al., 2020).

It is possible to estimate along-track displacements, which are sensitive to northward motions, by exploiting spectral diversity in the along-track, or azimuth, direction (Bechor & Zebker, 2006). This involves forming two sub-apertures for each SAR image, one with a look direction pointing slightly forwards and one pointing slightly backwards. Differencing interferograms formed from the forward-looking images and backward-looking images, results in phase change due to along-track displacement only, as displacement perpendicular to the flight direction cancels. The precision of these measurements is poor, however, as the difference in angle between the two sub-apertures is very small, particularly for the Interferometric Wideswath mode of Sentinel-1, which is the standard mode over land, due to the reduced Doppler spectrum available for each subswath.

The Terrain Observation with Progressive Scan (TOPS) approach that is used for the Interferometric Wideswath mode does, however, provide much greater spectral diversity in burst overlap regions, which are observed from two look angles differing by around 1°. Differencing backward-looking and forward-looking interferograms over the same burst overlap region allows estimation of along-track displacement with a precision of around 1 mm when averaged over whole overlap regions (Grandin et al., 2016).

Time series approaches have also been developed to estimate along-track velocities in the burst overlap regions (Hooper et al., 2020; Li et al., 2021). These studies treat the along-track velocities as relative measurements, but here we explore how accurately we can measure them in a global reference frame, as the along-track measurements are with respect to reference satellite positions, localized within the Earth-centered Earth-fixed framework of the ITRF2014.

We estimate the velocities in relatively large blocks containing, on average, 36 burst overlaps, in order to observe large-scale tectonic motion and characterize some of the error sources, such as the solid-earth tides and ionosphere, based on external models. In addition, we identify and correct systematic discrepancies in the along-track offset values related to a change in orbital ephemerides in mid-2020, and report differences between measurements from Sentinel-1A and Sentinel-1B satellites.

2. Estimating Along-Track Displacements

We extract the Level-1 single-look complex (SLC) data of the standard Sentinel-1 Interferometric Wide Swath burst units, and merge those bursts into larger spatial frames that we have defined. One typical frame consists of 13 bursts in each of the three subswaths and covers an area of approx. 250 × 250 km. We perform a standard procedure to coregister the SLC data for each acquisition toward a reference epoch (Lazecký et al., 2020). During this process, values of the mean subpixel shift in the azimuth direction, Δa, are estimated.

In detail, we use the Copernicus Sentinel-1 Precise Orbit Determination ephemerides to resample each SLC into the geometry of the reference epoch, considering topography with respect to the WGS-84 reference ellipsoid (Lazecký et al., 2020). We then run several iterations of intensity cross correlation to estimate a refined sub-pixel shift in both slant range (across-track) and azimuth (along-track), Δa_{ICC}, directions, with a precision below 0.01 pixels. Next, we resample the SLC to an intermediate product and iteratively estimate a further refined azimuth coregistration offset Δa_{SD} using spectral diversity of burst overlaps (De Zan & Monti Guarnieri, 2006).

Burst overlap areas are imaged with multiple lines of sight, and taking the difference between interferograms formed for each line of sight cancels the across-track displacement, leading to an estimate of the azimuth offset with expected precision below 0.0005 pixels. To ensure coherence, this offset is estimated between pairs of acquisitions close in time that have been resampled to the reference epoch, thus already shifted by their azimuth offset. The spectral diversity phase $\Delta\phi_{\mathrm{SD}}$ (Yagüe-Martínez et al., 2016) is related to azimuth pixel offset Δa_{SD} by

$$\Delta a_{\mathrm{SD}} = \frac{\Delta\phi_{\mathrm{SD}}\ PRF}{2\pi\Delta f_{DC}}, \tag{1}$$

where PRF = 486.486 Hz is the pulse repetition frequency (azimuth sampling rate) of the Sentinel-1 system, and Δf_{DC} is the Doppler centroid frequency difference in the burst overlap area.

We sum the subpixel offsets calculated from cross correlation and spectral diversity to give Δa values with respect to the reference frame of the orbit ephemerides, which since 16 February 2017, i.e., since version 1.3 of the precise orbit generating system (Peter et al., 2021a, 2021b), is the ITRF2014 realisation of the International Terrestrial Reference System. We extract relevant metadata per each frame, such as the average ground footprint heading angle, α, and the pixel resolution in the azimuth direction, r_{azi}. We use r_{azi} to convert the frame-wise azimuth pixel offsets, Δa, to the along-track displacement u_{az},

$$u_{az} = \Delta a\, r_{azi} = (\Delta a_{ICC} + \Delta a_{\mathrm{SD}})\, r_{azi}. \tag{2}$$

In total, we selected 107,476 Δa values from 1,063 LiCSAR frames, that have a minimum count of 30 Δa values per frame. As the LiCSAR processing currently concentrates on the Alpine-Himalayan orogenic belt (AHB), we

provide outputs of our analyses for both the full global data set and the AHB subset, defined by a bounding box of 25°W−110°W and 25°N−45°N.

3. Contributions to the Along-Track Displacement

Several factors contribute to displacement measured in the along track direction:

$$u_{az} = u_{az,tecton} + u_{az,tide} + u_{az,iono} + \varepsilon, \tag{3}$$

where $u_{\text{az,tecton}}$ is the motion due to tectonic displacement between acquisitions, $u_{\text{az,tide}}$ is displacement due to the difference in the solid-earth tides between acquisitions, $u_{\text{az,iono}}$ is due to the change in the along-track gradient of total electron content (TEC) between acquisitions, and ε is any residual due to orbit inaccuracies and noise. As our aim is to isolate $u_{\text{az,tecton}}$, we estimate and subtract values for $u_{\text{az,tide}}$ and $u_{\text{az,iono}}$.

3.1. Solid-Earth Tide Contribution

Solid-earth tides are calculated as the response to lunisolar gravitational attraction, computed from low-precision geocentric coordinates for the Moon and the Sun (Petit & Luzum, 2013), as implemented in the GMT software (Wessel et al., 2019). We expect the tide model to be sufficiently accurate for this analysis, although updated tide models exist, which also consider ocean tide loading or polar motion (Ducarme & Schüller, 2018; Martens et al., 2019).

We use the solid-earth tide model and calculate displacement in the along-track direction, $u_{\text{az,tide}}$, for the centre coordinates of each frame from the tidal components d_E, d_N in the east and north, respectively, using Equation 4.

$$u_{az,tide} = d_E \sin(\alpha) + d_N \cos(\alpha). \tag{4}$$

3.2. Ionospheric Contribution

For the ionospheric contribution to the along-track displacement, $u_{\text{az,iono}}$, we apply the IRI2016 model (Bilitza et al., 2017) that we consider sufficiently accurate for investigating seasonal fluctuations of u_{az} caused by ionospheric influence.

We use the inverse of the approach for estimating the ionospheric influence on spectral diversity values (Gomba et al., 2016), and estimate $u_{\text{az,iono}}$ based on modeled TEC between the satellite and the ground at the center of the frame, for two hypothetical forward-looking (A) and backward-looking (B) bursts, that is in a geometry similar to the solution of Liang et al. (2019).

Based on the look angle geometries, we calculate geographic coordinates of two ionosphere piercing points located in the line of sight toward the central point of the overlap between both hypothetical central bursts A, B at the altitude of the peak of ionospheric F2 layer, H_{iono}, extracted for each acquisition epoch by IRI2016. We then use IRI2016 to extract vertical TEC columns (TEC_v) between the ground and the approximate satellite altitude, at those coordinates and time.

Afterward, we estimate the average incidence angle below the ionosphere piercing points Θ_{IPP} (Ya'acob et al., 2010) and use it to convert the modeled TEC_v columns to the slant (line-of-sight) direction, TEC_s, as:

$$TEC_s = \frac{TEC_v}{\sqrt{1 - \sin\Theta_{IPP}{}^2}} = \frac{TEC_v}{\sqrt{1 - \left(\frac{R\sin\Theta}{R+H_{iono}}\right)^2}}, \tag{5}$$

where R is the radius of the Earth.

The SAR carrier wave of frequency f_0 is modulated by the Doppler effect from the satellite motion and the electronic beam steering during the TOPS acquisition mode, in the frequency range $f_A, f_B = f_0 \pm 0.5\Delta f_{\text{DC}}$ at the burst edges (Grandin et al., 2016). The phase advance ϕ_{iono} of an electromagnetic wave, oscillating in frequency f, induced during propagation through ionosphere is (Gomba et al., 2016):

$$\phi_{iono} = \frac{4\pi K}{c f} TEC, \tag{6}$$

where $K = 40.308193\ \frac{m^3}{s^2}$ is a constant for which we assume a commonly applied value (Hoque & Jakowski, 2012) and c is the speed of light in vacuum.

From Equation 5 of Yagüe-Martínez et al. (2016) and Equations 1, 2, and 6, we can derive the ionosphere-induced along-track displacement $u_{\text{az,iono}}$ toward the frame reference epoch as

$$u_{az,iono} = \frac{2\,PRF\,K}{c\,\Delta f_{DC}}\left(\frac{\Delta TEC_s(A)}{f_A} - \frac{\Delta TEC_s(B)}{f_B}\right) r_{azi}, \tag{7}$$

where $\Delta\text{TEC}_s(A, B)$ is the difference between the TEC_s estimates for the reference epoch and each acquisition in the line of sight toward the ground center of the overlap between bursts A and B, respectively. The difference of Doppler centroid frequencies for those lines of sight is $\Delta f_{\text{DC}} = f_A - f_B$. We use the average value of Δf_{DC}, as it varies between swaths (Grandin et al., 2016).

3.3. Impact of the Corrections

Figure 1 demonstrates the influence of the corrections applied to the original u_{az} values. The time series are generated from u_{az} values adjusted by the median value for each frame and filtered using a moving 10-sample median filter. Color represents the absolute latitude of each frame center, and shows how the ionospheric gradient is strongest at low latitudes and during ascending (evening) acquisitions. The seasonal nature of the tide and ionospheric corrections is also apparent, as well as a general decrease in ionospheric gradient between 2015 and 2019 as the solar cycle waned.

4. Effect of Updated Orbit Ephemerides

The orbit ephemerides products of Sentinel-1A and Sentinel-1B changed on 29th and 30 July 2020, respectively, to version 1.7, incorporating a correction of the on-board GPS antenna reference point position, as identified by Peter et al. (2020). This correction implied a 3-D position change of approximately 60 mm and led to a decrease in the root mean square error (RMSE) of the 3-D position of the satellites to below 10 mm (Peter et al., 2021a, 2021b). In the along-track direction of the satellite, the shift in the antenna reference point, d_{ARP}, is equal to 39 mm (Tables 3-1 and 3-2 in Fernández et al. (2019)).

We analyze our u_{az} values corrected for both solid-earth tides and ionosphere as described in Text S1 in Supporting Information S1, confirming the change in the orbit ephemeride products cause an offset of $d_{\text{ARP}} = -39$ mm, and we apply this correction.

As described in Texts S1.1 and S1.2 in Supporting Information S1, we additionally observe systematic offsets between both Sentinel-1A and Sentinel-1B satellites that are not a single value. As the apparent offsets between the 1A and 1B satellites have no consistent pattern and, as tested, using only one satellite would increase the overall standard error, we ignore these offsets. Yet, on the example of Maduo earthquake (Chen et al., 2021) in Text S1.1 in Supporting Information S1, we demonstrate that such offset must be considered to prevent misinterpretation as large-scale deformation.

Finally, we evaluate that the improved precision of satellite positioning by the updated orbits decreases RMSE of u_{az}-based estimates by 12%, or by median of 4.3 mm, in Text S1.3 in Supporting Information S1.

5. Estimation of Plate Motion

For the final velocity estimation, we invert the corrected data set of u_{az} values by linear regression with the Huber loss function (Huber, 2009), applied with parameters alpha = 1.0 and epsilon = 1.35, per frame. We calculate the mean square error, σ_u^2, assuming two degrees of freedom. We use the mean square error as an estimate of the variance for individual measurements and then apply Equation 8 to propagate the errors,

$$Q_m = \left[A^T Q_d^{-1} A\right]^{-1}, \tag{8}$$

where Q_m is the variance-covariance matrix of the model parameters, $Q_d^{-1} = 1/\sigma_u^2 I_N$ is the inverted N × N variance-covariance matrix of the measurements (I_N being the N × N identity matrix), and $A = [t_i, .., t_N; 1, .., 1]^T$ is an N × 2 matrix where t is the acquisition time in years. The first element of Q_m is the estimate of the variance of velocity σ_v^2. Estimates of velocities in ascending and descending tracks are plotted in Figure 2.

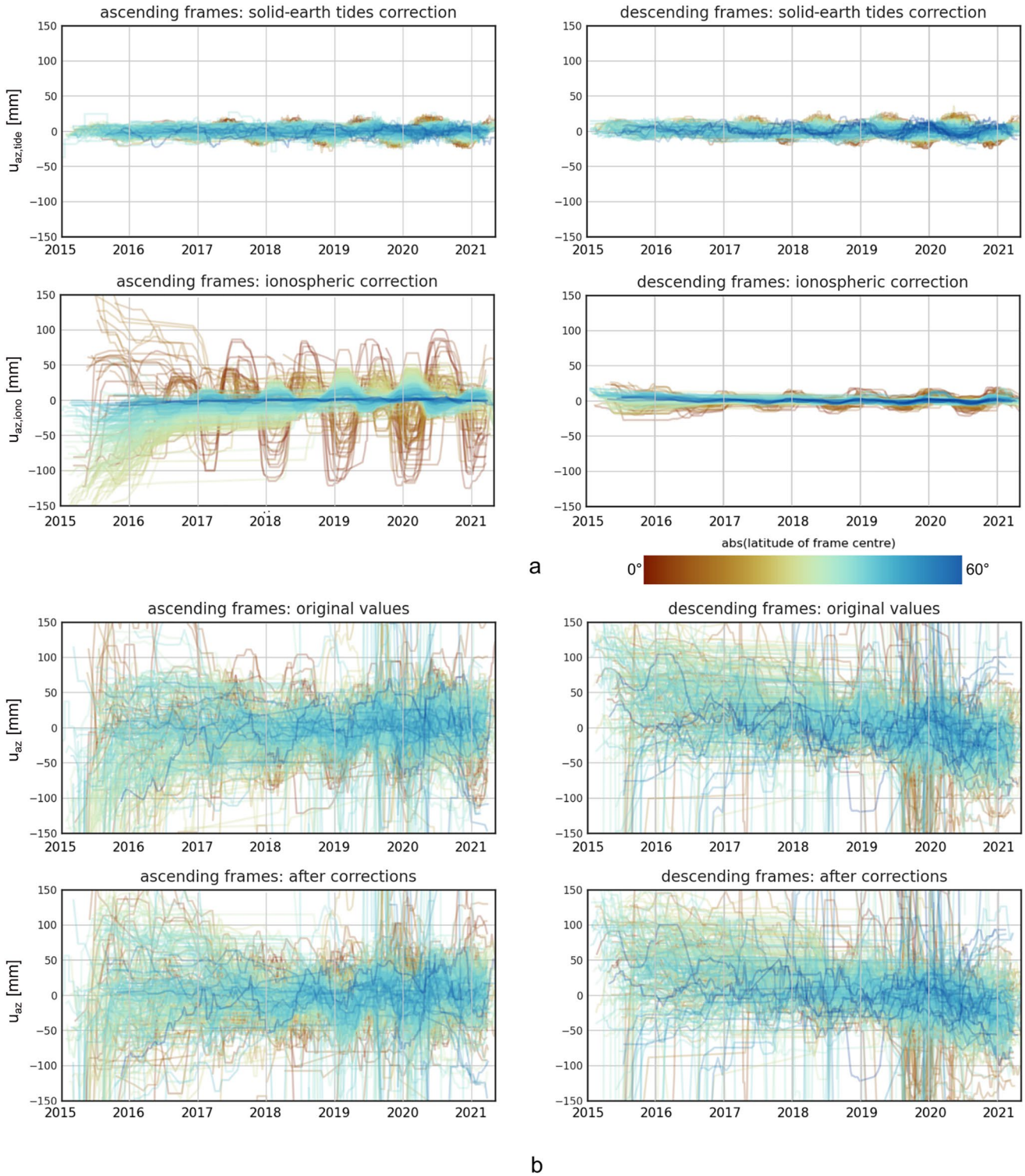

Figure 1. Influence of solid-earth tides and ionospheric corrections on time series of u_{az} values for, left, ascending and, right, descending frames; color gradient is based on distance from the Equator: (a) time series of modeled u_{az} corrections at the same scale; (b) u_{az} values before and after corrections. u_{az} values are after correction for updated orbits (see Section 4).

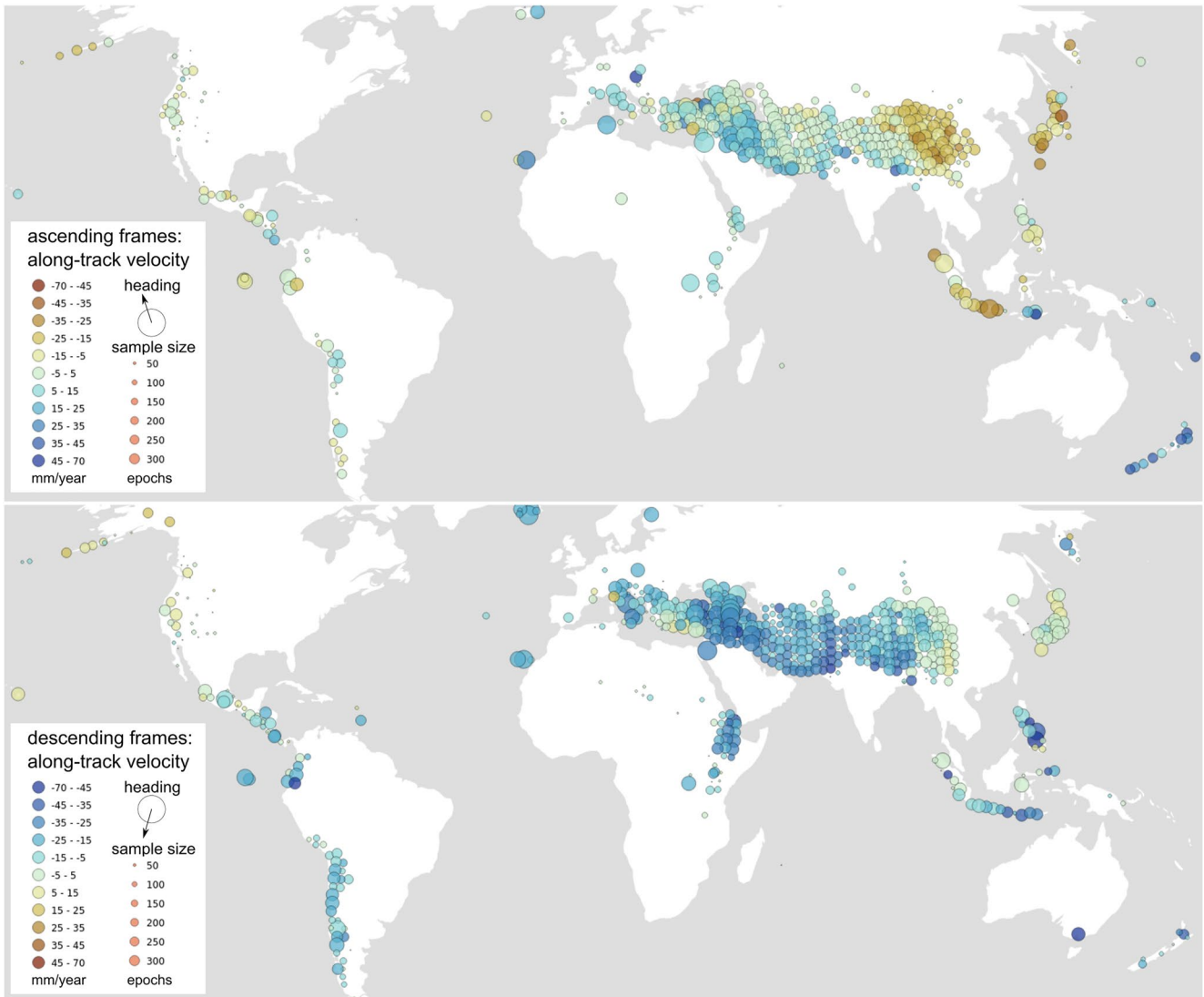

Figure 2. Global overview of along-track motion estimates extracted from ascending (top) and descending (bottom) tracks, after correction for both solid-earth tides and ionosphere. Projection: Robinson, EPSG: 54030.

Following modified procedures for line-of-sight decomposition (Wright et al., 2004), we decompose the final u_{az}-based estimates of horizontal displacement velocity, v, in the satellite azimuth direction from descending and ascending tracks, to eastwards and northwards direction components, v_E and v_N, respectively. We establish a global grid with a pixel size of approx. 250 × 250 km, map overlapping frames having their centroid inside the common grid cell, and calculate $v_{EN} = [v_E, v_N]^T$ for pixels with $v = \left[v_{D,1}..v_{D,i}..v_{A,1}..v_{A,j}\right]^T$ ($i > 0$, $j > 0$ being numbers of overlapping frames from descending and ascending tracks, respectively), by a least squares inversion of

$$v = A\, v_{EN}, \tag{9}$$

where matrix A contains look vector transformation coefficients per each of $n = i + j$ grouped frames as $A = [\sin\alpha_1..\sin\alpha_n, \cos\alpha_1..\cos\alpha_n]^T$. We evaluate the accuracy of the estimates using propagation of errors as before by Equation 8.

As the azimuth direction contains only a small component of eastwards motion, the eastwards velocity estimates are very sensitive to outliers. We therefore filter our data set of velocity estimates, removing 38 grid cells that have unreasonably large eastwards velocities, $|v_E| > 200$ mm/year, or RMSE, $\sigma_{v,E} > 50$ mm/year.

6. Evaluation of Results

6.1. Comparison to Reference Data

We first assess the accuracy of our global estimates by comparison with the ITRF2014 plate motion model (Altamimi et al., 2017) velocities, v_{PMM}, averaged per set of coordinates within each of the grid cells. We carry out a statistical evaluation of the quality of our estimates, noting that the extracted plate motion model velocities do not reflect actual ground motion in deforming plate boundary zones, leading to expected real differences between the two data sets.

We also perform the comparison over the Alpine-Himalayan Belt with velocities estimated from a global network of GPS measurements (Kreemer et al., 2014), v_{GPS}. The GPS measurements are provided in ITRF2008 no-net-rotation frame. We compare plate motion model velocities of ITRF2008, and observe that they differ by less than 0.5 mm/year on average from the ITRF2014 model over the Alpine-Himalayan Belt. The averaged GPS velocities and the plate motion model velocities differ on average by 8 mm/year northwards and 4 mm/year eastwards, in this plate boundary zone.

We first convert the reference velocities to the azimuth direction of the satellite measurements as in Equation 4 and compare to our along-track velocity estimates, grouped by direction of orbital tracks (ascending or descending). We then compare east-west and north-south velocities to our derived estimates.

6.2. Evaluation of the Final Accuracy

Median values of v and corresponding RMSE, σ_v, for both our full data set (253 grid cells) and the Alpine-Himalayan Belt subset (183 grid cells from 279 ascending and 255 descending frames) are given in Table 1, together with corresponding median values from reference datasets, $\tilde{v}_{PMM}$ and $\tilde{v}_{GPS}$.

The expected accuracy of our velocity estimates is given by their RMSE estimate. The final median 2-sigma error, $2\tilde{\sigma}_{v,tic}$, over the Alpine-Himalayan Belt is 3.6 mm/year northwards and 20.0 mm/year eastwards.

The median difference of velocities toward GPS estimates are reported in Table 1b. Our final estimates deviate from GPS by 13.4 mm/year eastwards and −8 mm/year northwards, on average. This is higher than we would expect from the supplied orbit errors and the expected precision of our measurements, but we note that these accuracy estimates also include errors in the GPS estimates, differences between ITRF2008 and 2014, errors introduced by differences in position between GPS and InSAR measurements, and residual ionospheric errors.

Table 1
Median Values of Estimated Velocities, $\tilde{v}$ [mm/Year], and Their Median Root Mean Square Error, $\tilde{\sigma}_v$ [mm/Year], Demonstrating Impact of Solid-Earth Tides and Ionospheric Corrections in (a) Global Data Set and (b) the Alpine-Himalayan Belt Subset

(a) Global data set [mm/year]				
Direction	$\tilde{v}_{PMM}$	$\tilde{v}_0 \pm \tilde{\sigma}_{v,0}$	$\tilde{v}_{tc} \pm \tilde{\sigma}_{v,tc}$	$\tilde{v}_{tic} \pm \tilde{\sigma}_{v,tic}$
Ascending track	0.0	3.4 ± 4.2	3.0 ± 4.1	1.3 ± 4.0
Descending track	−7.5	−10.2 ± 3.6	−10.0 ± 3.4	−9.9 ± 3.4
Eastwards	28.2	20.1 ± 13.5	22.1 ± 11.3	36.4 ± 11.4
Northwards	5.7	9.9 ± 2.6	9.2 ± 2.2	7.4 ± 2.1
(b) Alpine-Himalayan Belt subset [mm/year]				
Direction	$\tilde{v}_{GPS}$	$\tilde{v}_0 \pm \tilde{\sigma}_{v,0}$	$\tilde{v}_{tc} \pm \tilde{\sigma}_{v,tc}$	$\tilde{v}_{tic} \pm \tilde{\sigma}_{v,tic}$
Ascending track	10.4	6.6 ± 2.8	6.4 ± 2.7	1.5 ± 2.8
Descending track	−22.5	−16.0 ± 2.5	−16.5 ± 2.4	−16.7 ± 2.4
Eastwards	32.7	20.6 ± 12.1	25.9 ± 10.2	41.0 ± 10.0
Northwards	16.5	11.9 ± 2.2	12.1 ± 1.8	8.5 ± 1.8

Note. The subscript 0 refers to the original data set before the corrections, *tc* refers to tide-corrected and *tic* to tide- and ionosphere-corrected.

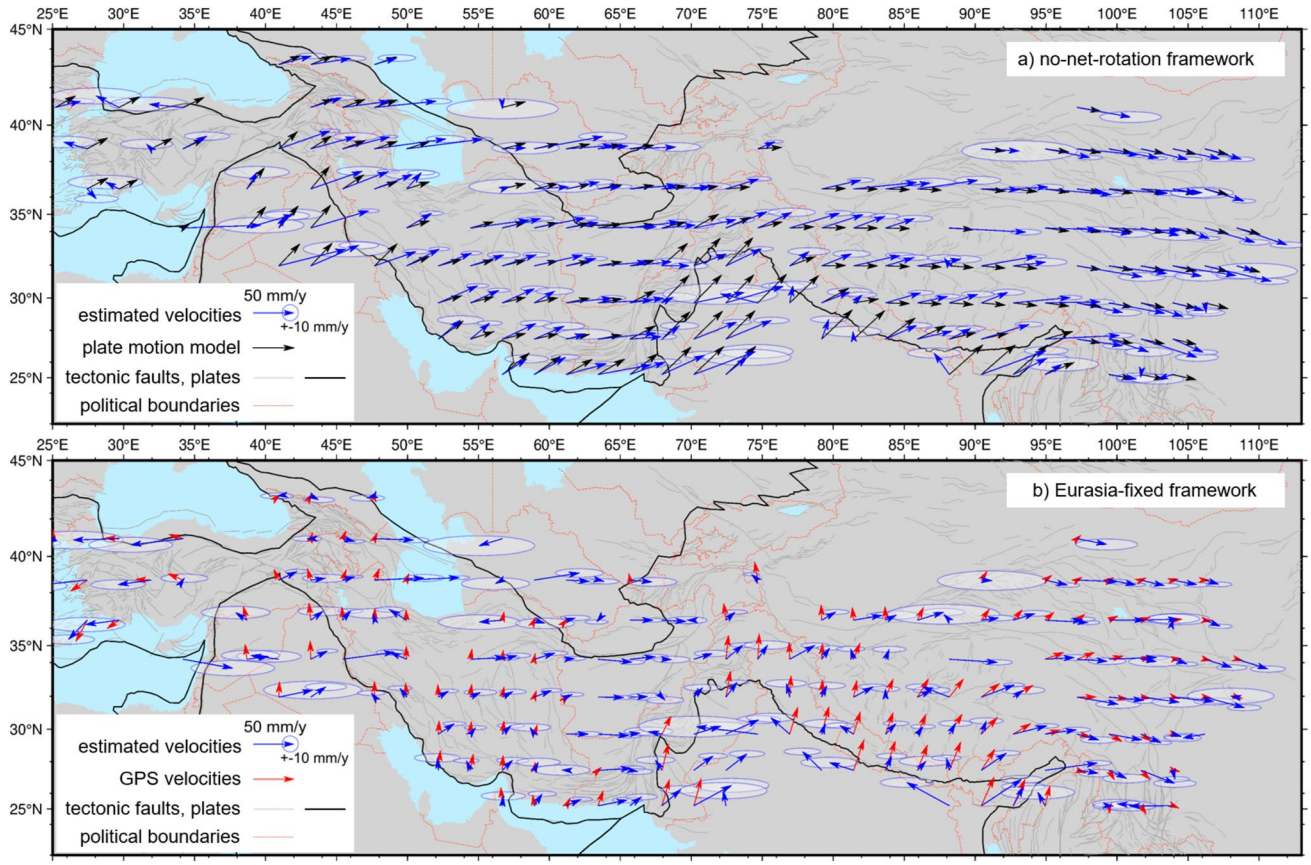

Figure 3. Comparison of our estimated velocity vectors over the Alpine-Himalayan Belt subset, corrected for solid-earth tides and ionosphere, to (a) the ITRF2014 plate motion model in no-net-rotation condition; and (b) GPS velocities (Kreemer et al., 2014) in Eurasia-fixed ITRF2014 reference frame. Error ellipses represent 2-σ (root mean square error) in respective directions, neglecting their possible correlation. Figure includes global active faults (Styron & Pagani, 2020) and tectonic plate boundaries (Hasterok et al., 2022).

6.3. Visualization of the Final Results

We visualize the horizontal velocities from our final u_{az}-based estimates after both solid-earth tide and ionosphere corrections and compare them to the ITRF2014 plate motion model in Figure 3a. We then convert our estimates to the Eurasia-fixed reference frame by subtracting the ITRF2014 no-net-rotation plate motion velocities and adding velocities in the Eurasia-fixed model, and compare to the GPS velocities provided in this frame by Kreemer et al. (2014), in Figure 3b.

The figure highlights expected spatial patterns of deviation from the plate motion model in deforming regions, for example, an increased westward motion of western Turkey (Weiss et al., 2020), but it also shows higher eastwards velocity of the eastern part of the Alpine-Himalayan Belt than measured by GPS, and other discrepancies.

7. Discussion

We extract along-track u_{az} estimates of large-scale deformation from averaged along-track pixel offsets Δa of Sentinel-1 data. The coregistration procedure refined by spectral diversity aims to estimate Δa with a precision of 0.0005 pixels, corresponding to u_{az} = 7 mm, although theoretically the method can reach precision below 1 mm (Grandin et al., 2016). The reliability of the estimate depends on interferometric coherence, which decreases with time. We therefore use previously resampled data close in time to estimate the spectral diversity, but estimation errors may thus propagate in time. We did not implement an approach to reduce the error propagation as in (Fattahi, Agram, & Simons, 2017).

The list of factors influencing u_{az} is not comprehensive (Gisinger et al., 2022; Yunjun et al., 2022). We limited our experiments to general models of solid-earth tides and ionosphere, the latter of which primarily affects ascending (dusk) frames, especially at lower latitudes. The accuracy of our velocity estimates significantly improves after incorporating corrections for solid-earth tides and ionospheric propagation, although we note large contributions to u_{az} values at the end of the Solar Cycle 24 that are not fully corrected (Figure 1).

An influence of the absolute magnitude of TEC is not expected to contribute to the along-track displacement estimate (Fattahi, Simons, & Agram, 2017; Gomba et al., 2016), yet it affects the intensity cross-correlation estimate that is then mitigated by spectral diversity, see Text S2 in Supporting Information S1. The ionospheric correction would benefit from separate estimation of its induced phase advance gradients per satellite sub-swath, which is planned future work, and also from TEC variation estimated from the interferometric phase (Gomba et al., 2016).

We also considered u_{az} due to troposphere delay gradients at the global mean height of water vapor (Bock et al., 2013) based on GACOS data (Yu et al., 2018), and decided to neglect this term, as it should induce less than 1 mm shift (see Text S1.1 in Supporting Information S1).

Our investigation on the updated orbits in version 1.7 (see Section 4 and Text S1 in Supporting Information S1) confirms that the updated orbit ephemeride products shift u_{az} values after the end of July 2020 by −39 mm. We estimate the offset as -35.5 ± 4.3 mm at 2-sigma error with a median value of −39 mm. Therefore, we apply this reported along-track offset of the GPS antenna reference point directly, in order to combine the u_{az} values with mixed orbits, without having to reprocess all data formed using the old orbits.

In Text S1 in Supporting Information S1, we also observe an increased model accuracy for u_{az} values using the updated, more accurate, orbits. The RMSE of described model decreased by 12% in median when using updated orbits. Thus, reprocessing data with the updated orbits would improve accuracy of our estimates.

In addition, we notice apparent offsets between Sentinel-1A and Sentinel-1B satellites that appear non-constant and unchanged after the update of orbits, see Figure S1 in Supporting Information S1. We observe no spatial pattern in these offsets. As our current data set contains relatively small amount of data values from Sentinel-1B, we could not reliably estimate this term, which therefore decreases accuracy of our velocity estimates.

Finally, we observe increased variance of data points before mid-2016, which often increases overall RMSE. Although an outlier detection technique was used to estimate velocities, an extended data set would allow dropping data from this time period while further improving the estimation accuracy.

8. Conclusions

We demonstrate the possibility of recovering accurate estimates of large-scale horizontal motion using along-track measurements of Sentinel-1 averaged over approximately 250 × 250 km cells. Such measurements can also be made at much higher resolution, albeit with lower accuracy.

The u_{az} estimates can be considered along-track measurements that are given in a global Earth-centered Earth-fixed no-net-rotation framework due to the GPS-based positioning of Sentinel-1 satellites. Our final u_{az}-based velocity estimates have median 2-sigma errors of 4 mm/year northwards and 23 mm/year eastwards (see Table 1). They fit reasonably well with the ITRF2014 plate motion model, although there are discrepancies, some of which are expected at plate boundary deformation zones, and some of which are not, such as extra eastwards motion over parts of the Alpine-Himalayan Belt.

Using averaged velocity estimates from GPS measurements over the Alpine-Himalayan Belt as reference, we identify a median bias of our estimates corresponding to 13.4 mm/year eastwards and −8.0 mm/year northwards, which is larger than we would expect, and further investigation into the cause is needed.

Accuracy can be further improved by incorporating better models of error sources, for example, an improved model of ionosphere (Galkin et al., 2022), or other sources of error (Gisinger et al., 2021) such as error due to bi-static satellite configuration, ocean tide loading or polar tide (Martens et al., 2019). Finally, accuracy can be further improved by reprocessing all data with the latest orbits and incorporating large-scale across-track (range) offset measurements, which have lower precision, but are more sensitive to east-west motion.

Data Availability Statement

We provide extracted data and estimates used within this article as an indexed Supporting information Data Set S1 and in a FAIR-compliant archive at Lazecký et al. (2022) [CC-4.0]. The software code for this research is available as Supporting information Data Set S2 as well as in Lazecký et al. (2022) [GNU GPL 3.0], and will be further updated in https://github.com/comet-licsar/daz [GNU GPL 3.0]. This work contains modified Copernicus Sentinel-1 data [2014–2021] available from https://scihub.copernicus.eu and Copernicus Sentinel-1 Precise Orbit Determination products available from Copernicus Sentinels POD Data Hub https://scihub.copernicus.eu/gnss. The data set of GPS measurements used in this research is included in the supplementary information files of Kreemer et al. (2014). The plate motion model values for ITRF2014 and ITRF2008 were extracted from the UNAVCO plate motion calculator at https://www.unavco.org/software/geodetic-utilities/plate-motion-calculator/plate-motion-calculator.html. We also used available open-source models to perform corrections on solid-earth tides (Wessel et al., 2019) and ionosphere (Bilitza et al., 2017). Figure 1 and Figure S1 in Supporting Information S1 were made with Matplotlib available under the Matplotlib license at https://matplotlib.org. Figure 2 was created using QGIS available under GNU GPL license at https://www.qgis.org. Figure 3 was created through PyGMT (Uieda et al., 2022) and includes data from (Styron & Pagani, 2020) and (Hasterok et al., 2022).

Acknowledgments
This work is based on data produced by COMET LiCSAR system, developed in support from The Natural Environment Research Council large grant, "Looking inside the continents from Space" (NE/K010867/1). COMET is the NERC Centre for the Observation and Modelling of Earthquakes, Volcanoes and Tectonics, a partnership between UK Universities and the British Geological Survey. This work contains modified Copernicus Sentinel-1 data [2014–2021] analysed by COMET LiCSAR system at JASMIN, the UK's collaborative data analysis environment (https://jasmin.ac.uk), and ARC4, part of the High Performance Computing facilities at the University of Leeds, UK. The authors wish to thank Dr. Heike Peter, Dr. Chris Rollins and Dr. Jonathan Weiss for helpful discussions.

References

Altamimi, Z., Métivier, L., Rebischung, P., Rouby, H., & Collilieux, X. (2017). ITRF2014 plate motion model. *Geophysical Journal International*, *209*(3), 1906–1912. https://doi.org/10.1093/gji/ggx136

Bechor, N. B. D., & Zebker, H. A. (2006). Measuring two-dimensional movements using a single inSAR pair. *Geophysical Research Letters*, *33*(16), L16311. https://doi.org/10.1029/2006GL026883

Bilitza, D., Altadill, D., Truhlik, V., Shubin, V., Galkin, I., Reinisch, B., & Huang, X. (2017). International reference ionosphere 2016: From ionospheric climate to real-time weather predictions. *Space Weather*, *15*(2), 418–429. https://doi.org/10.1002/2016SW001593

Bock, O., Bosser, P., Bourcy, T., David, L., Goutail, F., Hoareau, C., et al. (2013). Accuracy assessment of water vapour measurements from in situ and remote sensing techniques during the DEMEVAP 2011 campaign at OHP. *Atmospheric Measurement Techniques*, *6*(10), 2777–2802. https://doi.org/10.5194/amt-6-2777-2013

Chen, H., Qu, C., Zhao, D., Ma, C., & Shan, X. (2021). Rupture kinematics and coseismic slip model of the 2021 mw 7.3 Maduo (China) earthquake: Implications for the seismic hazard of the Kunlun fault. *Remote Sensing*, *13*(16), 3327. https://doi.org/10.3390/rs13163327

De Zan, F., & Monti Guarnieri, A. (2006). TOPSAR: Terrain observation by progressive scans. *IEEE Transactions on Geoscience and Remote Sensing*, *44*(9), 2352–2360. https://doi.org/10.1109/TGRS.2006.873853

Ducarme, B., & Schüller, K. (2018). Canonical wave grouping as the key to optimal tidal analysis. *Bulletin d'Informations Marees Terrestres (BIM)*, *150*, 12131–12244.

Fattahi, H., Agram, P., & Simons, M. (2017a). A network-based enhanced spectral diversity approach for tops time-series analysis. *IEEE Transactions on Geoscience and Remote Sensing*, *55*(2), 777–786. https://doi.org/10.1109/TGRS.2016.2614925

Fattahi, H., Simons, M., & Agram, P. (2017b). InSAR time-series estimation of the ionospheric phase delay: An extension of the split range-spectrum technique. *IEEE Transactions on Geoscience and Remote Sensing*, *55*(10), 5984–5996. https://doi.org/10.1109/TGRS.2017.2718566

Fernández, M., Aguilar, J. A., & Fernández, J. (2019). Sentinel-1 properties for GPS pod: Copernicus sentinel-1, -2, and -3 precise orbit determination service (sentinelspod). Retrieved from https://sentinels.copernicus.eu/documents/247904/3455957/Sentinel-1-properties-for-GPS-POD

Galkin, I., Froń, A., Reinisch, B., Hernández-Pajares, M., Krankowski, A., Nava, B., et al. (2022). Global monitoring of ionospheric weather by GIRO and GNSS data fusion. *Atmosphere*, *13*(3), 371. https://doi.org/10.3390/atmos13030371

Gisinger, C., Libert, L., Marinkovic, P., Krieger, L., Larsen, Y., Valentino, A., et al. (2022). The extended timing annotation dataset for sentinel-1—Product description and first evaluation results. *IEEE Transactions on Geoscience and Remote Sensing*, *60*, 1–22. https://doi.org/10.1109/TGRS.2022.3194216

Gisinger, C., Schubert, A., Breit, H., Garthwaite, M., Balss, U., Willberg, M., et al. (2021). In-depth verification of sentinel-1 and TerraSAR-x geolocation accuracy using the Australian corner reflector array. *IEEE Transactions on Geoscience and Remote Sensing*, *59*(2), 1154–1181. https://doi.org/10.1109/TGRS.2019.2961248

Gomba, G., Parizzi, A., De Zan, F., Eineder, M., & Bamler, R. (2016). Toward operational compensation of ionospheric effects in sar interferograms: The split-spectrum method. *IEEE Transactions on Geoscience and Remote Sensing*, *54*(3), 1446–1461. https://doi.org/10.1109/TGRS.2015.2481079

Grandin, R., Klein, E., Métois, M., & Vigny, C. (2016). Three-dimensional displacement field of the 2015 mw8.3 illapel earthquake (Chile) from across- and along-track sentinel-1 tops interferometry. *Geophysical Research Letters*, *43*(6), 2552–2561. https://doi.org/10.1002/2016GL067954

Hasterok, D., Halpin, J. A., Collins, A. S., Hand, M., Kreemer, C., Gard, M. G., & Glorie, S. (2022). New maps of global geological provinces and tectonic plates. *Earth-Science Reviews*, *231*, 104069. https://doi.org/10.1016/j.earscirev.2022.104069

Hooper, A. J., Piromthong, P., Elliott, J. R., Weiss, J. R., & Lazecký, M. (2020). The improvement to high-resolution maps of interseismic strain accumulation from incorporating Sentinel-1 along-track measurements. In *AGU fall meeting abstracts* (Vol. 2020, pp. G018–G007).

Hoque, M., & Jakowski, N. (2012). Ionospheric propagation effects on GNSS signals and new correction approaches. *Global navigation satellite systems: signal, theory and applications*, *10*, 30090. https://doi.org/10.5772/30090

Huber, P. (2009). *Robust statistics*. Wiley.

Kreemer, C., Blewitt, G., & Klein, E. C. (2014). A geodetic plate motion and global strain rate model. *Geochemistry, Geophysics, Geosystems*, *15*(10), 3849–3889. https://doi.org/10.1002/2014GC005407

Lazecký, M., Hooper, A., & Piromthong, P. (2022). InSAR-derived horizontal velocities in a global reference frame. [Dataset, Software]. Zenodo. https://doi.org/10.5281/zenodo.7730391

Lazecký, M., Spaans, K., González, P. J., Maghsoudi, Y., Morishita, Y., Albino, F., et al. (2020). LiCSAR: An automatic InSAR tool for measuring and monitoring tectonic and volcanic activity. *Remote Sensing*, *12*(15), 2430. https://doi.org/10.3390/rs12152430

Li, X., Jónsson, S., & Cao, Y. (2021). Interseismic deformation from sentinel-1 burst-overlap interferometry: Application to the southern dead sea fault. *Earth and Space Science Open Archive*, *13*. e2021GL093481. https://doi.org/10.1002/essoar.10506585.1

Liang, C., Agram, P., Simons, M., & Fielding, E. J. (2019). Ionospheric correction of inSAR time series analysis of c-band sentinel-1 tops data. *IEEE Transactions on Geoscience and Remote Sensing*, *57*(9), 6755–6773. https://doi.org/10.1109/TGRS.2019.2908494

Martens, H. R., Rivera, L., & Simons, M. (2019). LoadDef: A python-based toolkit to model elastic deformation caused by surface mass loading on spherically symmetric bodies. *Earth and Space Science*, *6*(2), 311–323. https://doi.org/10.1029/2018EA000462

Peter, H., Fernández, J., & Féménias, P. (2020). Copernicus sentinel-1 satellites: Sensitivity of antenna offset estimation to orbit and observation modelling. *Advances in Geosciences*, *50*, 87–100. https://doi.org/10.5194/adgeo-50-87-2020

Peter, H., Fernández, M., Arnold, D., Duan, B., Simons, W., Gini, F., et al. (2021). Copernicus POD service - orbit reprocessing for Copernicus sentinel-1 satellites. In *EGU general assembly conference abstracts*. EGU21-5296.

Peter, H., Usón, M. F., Aguilar, J. A., & Fernández, J. (2021b). Copernicus pod product handbook: Copernicus sentinel-1, -2 and -3 precise orbit determination service (cpod). Retrieved from https://sentinels.copernicus.eu/documents/247904/3372484/Sentinels-POD-Product-Handbook-1.19.pdf

Petit, G., & Luzum, B. (2013). The 2010 reference edition of the IERS conventions. In Z. Altamimi & X. Collilieux (Eds.), *Reference frames for applications in geosciences* (pp. 57–61). Springer Berlin Heidelberg.

Styron, R., & Pagani, M. (2020). The gem global active faults database. *Earthquake Spectra*, *36*(1_suppl), 160–180. https://doi.org/10.1177/8755293020944182

Uieda, L., Tian, D., Leong, W. J., Jones, M., Schlitzer, W., Grund, M., et al. (2022). PyGMT: A Python interface for the generic mapping tools. [Software]. Zenodo. (The development of PyGMT has been supported by NSF grants OCE-1558403 and EAR-1948603). https://doi.org/10.5281/zenodo.6426493

Weiss, J. R., Walters, R. J., Morishita, Y., Wright, T. J., Lazecký, M., Wang, H., et al. (2020). High-resolution surface velocities and strain for Anatolia from sentinel-1 inSAR and GNSS data. *Geophysical Research Letters*, *47*(17), e2020GL087376. https://doi.org/10.1029/2020GL087376

Wessel, P., Luis, J. F., Uieda, L., Scharroo, R., Wobbe, F., Smith, W. H. F., & Tian, D. (2019). The generic mapping tools version 6. *Geochemistry, Geophysics, Geosystems*, *20*(11), 5556–5564. https://doi.org/10.1029/2019GC008515

Wright, T. J., Parsons, B. E., & Lu, Z. (2004). Toward mapping surface deformation in three dimensions using inSAR. *Geophysical Research Letters*, *31*(1), L01607. https://doi.org/10.1029/2003GL018827

Ya'acob, N., Abdullah, M., & Ismail, M. (2010). Gps total electron content (TEC) prediction at ionosphere layer over the equatorial region. https://doi.org/10.5772/8474

Yagüe-Martínez, N., Prats-Iraola, P., Rodríguez González, F., Brcic, R., Shau, R., Geudtner, D., et al. (2016). Interferometric processing of sentinel-1 tops data. *IEEE Transactions on Geoscience and Remote Sensing*, *54*(4), 2220–2234. https://doi.org/10.1109/TGRS.2015.2497902

Yu, C., Li, Z., Penna, N. T., & Crippa, P. (2018). Generic atmospheric correction model for interferometric synthetic aperture radar observations. *Journal of Geophysical Research: Solid Earth*, *123*(10), 9202–9222. https://doi.org/10.1029/2017JB015305

Yunjun, Z., Fattahi, H., Pi, X., Rosen, P., Simons, M., Agram, P., & Aoki, Y. (2022). Range geolocation accuracy of C-/L-Band SAR and its implications for operational stack coregistration. *IEEE Transactions on Geoscience and Remote Sensing*, *60*, 1–19. https://doi.org/10.1109/TGRS.2022.3168509